

*Aerosol and cloud microphysics
covariability in the northeast Pacific
boundary layer estimated with ship-based
and satellite remote sensing observations*

Article

Published Version

Painemal, D., Chiu, J.-Y. C., Minnis, P., Yost, C., Zhou, X., Cadeddu, M., Eloranta, E., Lewis, E. R., Ferrare, R. and Kollias, P. (2017) Aerosol and cloud microphysics covariability in the northeast Pacific boundary layer estimated with ship-based and satellite remote sensing observations. *Journal of Geophysical Research: Atmospheres*, 122 (4). pp. 2403-2418. ISSN 2169-8996 doi: <https://doi.org/10.1002/2016JD025771> Available at <http://centaur.reading.ac.uk/69505/>

It is advisable to refer to the publisher's version if you intend to cite from the work.

To link to this article DOI: <http://dx.doi.org/10.1002/2016JD025771>

Publisher: American Geophysical Union

All outputs in CentAUR are protected by Intellectual Property Rights law, including copyright law. Copyright and IPR is retained by the creators or other copyright holders. Terms and conditions for use of this material are defined in

the [End User Agreement](#).

www.reading.ac.uk/centaur

CentAUR

Central Archive at the University of Reading

Reading's research outputs online

RESEARCH ARTICLE

10.1002/2016JD025771

Key Points:

- Satellite and ship-based remote sensing cloud retrievals are used to calculate the aerosol-cloud covariability in the NE Pacific
- CCN, accumulation mode aerosol, and extinction coefficient yield consistently high covariability, near the physical upper limit
- Computed aerosol-cloud interaction is consistent with aircraft studies in the eastern Pacific, especially for well-mixed boundary layers

Correspondence to:

D. Painemal,
david.painemal@nasa.gov

Citation:

Painemal, D., J.-Y. C. Chiu, P. Minnis, C. Yost, X. Zhou, M. Cadetdu, E. Eloranta, E. R. Lewis, R. Ferrare, and P. Kollias (2017), Aerosol and cloud microphysics covariability in the northeast Pacific boundary layer estimated with ship-based and satellite remote sensing observations, *J. Geophys. Res. Atmos.*, 122, doi:10.1002/2016JD025771.

Received 10 AUG 2016

Accepted 13 FEB 2017

Accepted article online 14 FEB 2017

Aerosol and cloud microphysics covariability in the northeast Pacific boundary layer estimated with ship-based and satellite remote sensing observations

David Painemal^{1,2} , J.-Y. Christine Chiu³ , Patrick Minnis² , Christopher Yost¹ , Xiaoli Zhou⁴ , Maria Cadetdu⁵ , Edwin Eloranta⁶ , Ernie R. Lewis⁷ , Richard Ferrare² , and Pavlos Kollias⁸ 

¹Science Systems and Applications, Inc., Hampton, Virginia, USA, ²NASA Langley Research Center, Hampton, Virginia, USA,

³Department of Meteorology, University of Reading, Reading, UK, ⁴Department of Atmospheric and Oceanic Sciences, McGill University, Montreal, Quebec, Canada, ⁵Environmental Science Division, Argonne National Laboratory, Lemont, Illinois, USA, ⁶Space Science and Engineering Center, University of Wisconsin-Madison, Madison, Wisconsin, USA,

⁷Brookhaven National Laboratory, Upton, New York, USA, ⁸School of Marine and Atmospheric Sciences, Stony Brook University, Stony Brook, New York, USA

Abstract Ship measurements collected over the northeast Pacific along transects between the port of Los Angeles (33.7°N, 118.2°W) and Honolulu (21.3°N, 157.8°W) during May to August 2013 were utilized to investigate the covariability between marine low cloud microphysical and aerosol properties. Ship-based retrievals of cloud optical depth (τ) from a Sun photometer and liquid water path (LWP) from a microwave radiometer were combined to derive cloud droplet number concentration N_d and compute a cloud-aerosol interaction (ACI) metric defined as $ACI_{CCN} = \partial \ln(N_d) / \partial \ln(CCN)$, with CCN denoting the cloud condensation nuclei concentration measured at 0.4% ($CCN_{0.4}$) and 0.3% ($CCN_{0.3}$) supersaturation. Analysis of $CCN_{0.4}$, accumulation mode aerosol concentration (N_a), and extinction coefficient (σ_{ext}) indicates that N_a and σ_{ext} can be used as $CCN_{0.4}$ proxies for estimating ACI. ACI_{CCN} derived from 10 min averaged N_d and $CCN_{0.4}$ and $CCN_{0.3}$, and $CCN_{0.4}$ regressions using N_a and σ_{ext} , produce high ACI_{CCN} : near 1.0, that is, a fractional change in aerosols is associated with an equivalent fractional change in N_d . ACI_{CCN} computed in deep boundary layers was small ($ACI_{CCN} = 0.60$), indicating that surface aerosol measurements inadequately represent the aerosol variability below clouds. Satellite cloud retrievals from MODerate-resolution Imaging Spectroradiometer and GOES-15 data were compared against ship-based retrievals and further analyzed to compute a satellite-based ACI_{CCN} . Satellite data correlated well with their ship-based counterparts with linear correlation coefficients equal to or greater than 0.78. Combined satellite N_d and ship-based $CCN_{0.4}$ and N_a yielded a maximum $ACI_{CCN} = 0.88$ – 0.92 , a value slightly less than the ship-based ACI_{CCN} , but still consistent with aircraft-based studies in the eastern Pacific.

1. Introduction

The aerosol indirect effect (AIE) in low marine clouds remains a central source of uncertainty in climate models, hampering our ability to accurately quantify anthropogenic radiative forcing [e.g., Rosenfeld *et al.*, 2014; Carslaw *et al.*, 2013, and references therein]. Reduction of AIE intermodel spread thus requires accurate measurements of cloud and aerosol properties that can guide future improvements in model parameterizations. However, the use of AIE estimates from observations is challenging because different platforms can yield a broad range of AIE values [e.g., McComiskey and Feingold, 2008]. While this variability can be partially due to the unique atmospheric characteristics of the cloud regimes sampled (e.g., maritime versus continental), less attention has been paid to the physical representativeness of the observations. In fact, even when the measurements are accurate within some tolerable errors, different aerosol measurements might not yield the same covariability with the cloud microphysics. Since the property that is most directly linked to cloud droplet formation is ultimately cloud condensation nuclei (CCN) concentration, the suitability of other aerosol measurements depends on how well they can reproduce CCN concentration variability. For instance, Shinozuka *et al.* [2015] show a close correlation between CCN concentration and aerosol extinction coefficient over the oceans, with fractional changes in extinction yielding smaller fractional changes in CCN concentration. Similarly, attempts have been made to use aerosol optical depth (AOD) as a proxy for CCN concentration [e.g., Andreae, 2009]. Although CCN concentration and AOD correlate well when considering

a broad range of aerosol concentrations, the relationship is poorly characterized in pristine maritime environments [e.g., *Andreae*, 2009, Figure 1], likely because of a few large aerosol particles that contribute little to CCN concentration but dominate the AOD. This is particularly troublesome as it is common to use satellite-based AOD for evaluating AIE model performance [e.g., *Quaas et al.*, 2009]. Interestingly, *Painemal and Zuidema* [2010] and *Painemal et al.* [2015] show that the combined use of satellite cloud microphysics and in situ CCN concentration can produce robust correlations in cloud-topped marine boundary layers. Nevertheless, consistency between ground-based and satellite-based remote sensing estimates of AIE has not been investigated with the necessary detail.

For better observational quantification of AIE, it would be desirable to adopt a regional focus and rely on the redundancy and consistency of both instruments and retrievals. By adopting a regional focus, one can better isolate the meteorological processes and aerosol chemical properties that dictate changes in the aerosol-cloud covariability. Redundancy, on the other hand, will help determine the robustness of the observations and help evaluate the advantages of different aerosol and cloud proxies. Although these requirements are met by the multiobservational platforms deployed by the Atmospheric Radiation Measurement (ARM) program [e.g., *Miller et al.*, 2016], long-term observations over marine environments have been elusive until a recent ARM field campaign over the northeast Pacific: the Marine ARM GPCI (Global Energy and Water Cycle Experiment (GEWEX) Cloud System Study (GCSS) Pacific cross-section intercomparison) Investigation of Clouds (MAGIC) campaign [*Lewis and Teixeira*, 2015; *Zhou et al.*, 2015]. MAGIC deployed the second ARM mobile facility (AMF2) on board a cargo ship, the *Horizon Spirit*, that sailed between the ports of Los Angeles, California (33.7°N, 118.2°W) and Honolulu, Hawaii (21.3°N, 157.8°W) during two observation periods: September (2012)–January (2013) and May–September of 2013. AMF2 included a suite of aerosol probes that measured surface CCN concentration, aerosol size distribution, and aerosol light scattering; radiometric instrumentation for cloud retrievals; a high spectral resolution lidar (HSRL); and Ka band and W band radars [e.g., *Kollias et al.*, 2016].

This work builds on a recent article [*Painemal et al.*, 2015, hereinafter P15] that describes seasonal changes and synoptic patterns that influence aerosol and cloud microphysics variability during MAGIC. Here we follow a more specific focus by centering our efforts on quantifying the covariability and the cloud-aerosol interaction metric $ACI_{\alpha} = \partial \ln(N_d) / \partial \ln(\alpha)$ between different aerosols properties (α) and cloud droplet number concentration (N_d) by utilizing MAGIC in situ and remote sensors as well as satellite observations during Spring-Summer of 2013.

2. Data Set

We make extensive use of numerous MAGIC observations, which encompass standard meteorological observations and radiosondes, along with specific instrumentation unique to this deployment, which included passive and active remote sensors. We also complemented the ship data with retrievals from two satellite sensors, the Fifteenth Geostationary Operational Environmental Satellite (GOES-15) imager and the MODerate-resolution Imaging Spectroradiometer (MODIS) on the Terra and Aqua satellites. The data sets are described below and summarized in Table 1.

2.1. Ship-Based Aerosol Observations:

Cloud condensation nuclei concentrations were measured with a CCN counter [*Roberts and Nenes*, 2005] manufactured by Droplet Measurements Technology (DMT). The CCN counter varies supersaturations from 0% to 0.6% every 10 min. CCN concentrations at 0.4% were primarily used in this study, with additional analyses of 0.3% and 0.2% supersaturation CCN. These supersaturation values are consistent with the 0.3% used by *Hegg et al.* [2012], based on aircraft observations in California coastal stratocumulus clouds reported by *Hudson et al.* [2010]. Dry aerosol size distributions were measured with the DMT Ultrahigh Sensitivity Aerosol Spectrometer (UHSAS), which is a laser-based optical scattering, aerosol particle spectrometer that sizes aerosol particles with optical diameter between 60 and 1000 nm in 100 equally spaced logarithmic bins by the amount of light they scatter into given angular regions from a 1054 nm laser [*Cai et al.*, 2008]. Aerosol light scattering was measured at three wavelengths: 450, 550, and 750 nm, with a TSI Integrating Nephelometer model 3563 [*Anderson et al.*, 1996] that alternately sampled particles with aerodynamic diameters less than 1 and 10 μm . Aerosol light absorption was measured by a particle soot absorption photometer (PSAP, manufactured by Radiance Research, Inc.) at 470, 522, and 660 nm based on optical

Table 1. Instruments and Associated Measurements/Retrievals

Instrument	Measurements/Retrievals
CCN particle counter	CCN concentrations at different supersaturations from 0 to 0.6%
Cimel Sun photometer	Cloud optical depth (τ), effective radius (r_e), liquid water path (LWP), and cloud droplet number concentration (N_d , equation (2))
Ultrahigh sensitivity aerosol spectrometer (UHSAS)	Aerosol size distribution, accumulation mode dry aerosol concentration (N_{or} , diameters between 0.1 and 1.0 μm)
Nephelometer	Aerosol scattering coefficient at wavelengths 450, 550, and 700 nm; instrument alternates measurements for particles with aerodynamic diameters less than 1 μm and less than 10 μm .
Particle soot absorption photometer (PSAP)	Aerosol absorption coefficient (σ_{abs}) at wavelengths 470, 522, and 660 nm; instrument alternates measurements for particles with aerodynamic diameters less than 1 μm and less than 10 μm .
Three-channel microwave radiometer	Liquid water path and N_d (equation (2))
K band radar	Cloud layers detection, cloud top height, and precipitation flag
University of Wisconsin's high spectral resolution lidar (HSRL)	Cloud base height detection and aerosol backscatter cross section (σ_{back})
Ceilometer	Cloud base height detection and cloud frequency of occurrence
GOES-15 satellite imager	Daytime r_e and τ ; N_d derived from equation (3)
MODIS (Aqua and Terra satellites)	Daytime r_e and τ ; N_d derived from equation (3)

transmittance measurements through a glass/cellulose filter over time as particles are deposited. The data, obtained for aerodynamic diameters less than 1 and 10 μm , are corrected for scattering and filter loading as described in *Bond et al.* [1999]. We adjusted the PSAP absorption to the nephelometer wavelength of 550 nm using the Ångström exponent determined from measurements at 470 and 660 nm, that is, assuming linearity between the logarithm of the absorption coefficient and logarithm of the wavelength. The University of Wisconsin High Spectral Resolution Lidar (HSRL) [*Eloranta*, 2005] provided information about the vertical distribution of aerosols and cloud boundary detection. The instrument operates at a 532 nm wavelength, with a field of view of 100 μrad and a range resolution of 7.5 m. Here we utilize the particle backscatter cross section because it is a robust retrieval and not strongly affected by calibration issues and signal noise.

2.2. Ship-Based Cloud Observations

Liquid water path was retrieved from a three-channel microwave radiometer (MWR), with a 3° field of view and three channels at 23.83, 30, and 89 GHz, with the last providing further constraint that enables retrieving more accurate LWP for thin clouds. These retrievals, based on iterative radiative calculations under an optimal estimation framework [*Cadeddu et al.*, 2013], have been recently used for evaluating satellite microwave liquid water and water vapor paths [*Painemal et al.*, 2016]. The effect of the ship motion was accounted for in the instrument calibration. Moreover, given the instrument's relatively large field of view, and typical angular departures from zenith were less than 1° [*Chiu et al.*, 2016], the ship motion effects in the MWR measurements are deemed small.

Cloud base height was determined from a Vaisala CL31 laser ceilometer and the HSRL with vertical resolution of 7.5 m, using for the latter a particle backscatter cross-section threshold of $1 \cdot 10^{-4} \text{m}^{-1} \text{sr}^{-1}$, as in *Fielding et al.* [2015]. Cloud frequency was defined from the ceilometer as the ratio of the number of cloudy samples to the total. Cloud top height and precipitation detection were derived from a K band radar as in *Zhou et al.* [2015] using a hydrometeor mask algorithm based on the methodology by *Hildebrand and Sekhon* [1974] for the determination of noise level. The K band radar's high temporal resolution of 0.4 s oversampled the ship motion, allowing compensation of the motion effect by averaging the radar data to 4 s [*Zhou et al.*, 2015]. A precipitation event is defined for times when an echo was detected in the lowest radar gate (~150 m). This definition encompasses both rain and drizzle events according to the definitions in *Zhou et al.* [2015]. The analysis was limited to samples in which the radar detected cloud top heights below 3 km, even though the frequency of occurrence of higher clouds is less than 4.1% per month during the period of study.

A narrow field-of-view (1.2°) Cimel Sun photometer was utilized to retrieve cloud optical thickness (τ) and effective radius (r_e), with optimal operation during May, June, and the first two transects of July. Unlike Sun photometers in the Aerosol Robotic Network that operate in the normal aerosol mode for retrieving aerosol optical depth, the one deployed in MAGIC ran in cloud mode, that is, viewing zenith. The analysis method, described in *Chiu et al.* [2010, 2012], uses zenith radiances at wavelengths of 440, 870, and 1640 nm and

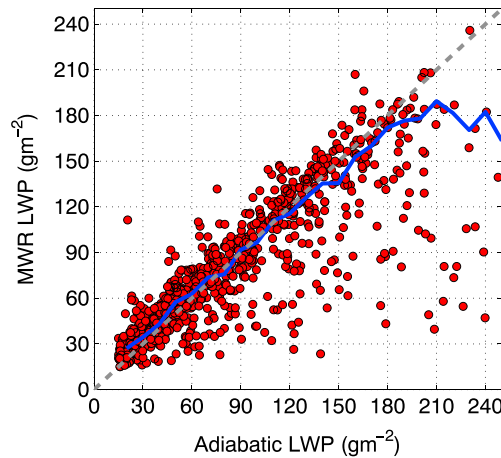


Figure 1. Ten-minute average MWR-determined LWP and adiabatic LWP for June and July of 2013. Blue line is the median MWR LWP as a function of its adiabatic counterpart with bin widths of 15 g/m^2 . The gray dashed line denotes the 1:1 relationship.

retrieves τ and r_e through minimizing the errors between the observed radiances and a lookup table constructed using a plane-parallel radiative transfer model for different values of r_e and τ . The actual instrument pointing angle was geometrically derived using the ship navigation data [Chiu *et al.*, 2016]. Assuming a cloud profile with a constant cloud droplet number concentration and linearly increasing effective radius with height, LWP can then be indirectly estimated as $LWP = \frac{5}{9} \rho_w r_e \tau$, with ρ_w denoting the liquid water density. This assumption for the cloud vertical structure is supported by aircraft observations off the coast of California during the 2005 Marine Stratus/Stratocumulus Experiment (MASE) campaign [Wang *et al.*, 2009]. Since independent LWP retrievals are available from MWR during MAGIC, we will evaluate the water content stratification assumption by comparing MWR LWP with its adiabatic counterpart in section 3.

2.3. Satellite Cloud Retrievals

Standard satellite retrievals for MAGIC are described in P15 and briefly summarized here. Cloud property retrievals were derived from the GOES-15 imager and the MODIS on the Terra and Aqua satellites. Retrievals of τ , r_e , cloud temperature, and cloud cover were produced using algorithms designed for MODIS for the Clouds and Earth's Radiant Energy System (CERES) project Edition 4 products [Minnis *et al.*, 2010, 2011] and adapted to GOES-15 [Minnis *et al.*, 2008]. Satellite LWP was computed as $LWP = \frac{5}{9} \rho_w r_e \tau$. While good agreement between aircraft observations and MODIS and GOES is reported in Zheng *et al.* [2011] and Painemal *et al.* [2012] for the southeast Pacific, we will further extend the comparison with the use of ship-based observations.

3. Adiabaticity and N_d Calculation

One basic assumption in estimating both N_d and LWP from visible/near-infrared ship and satellite-based retrievals is that the cloud liquid water content linearly increases with height. We tested this assumption by comparing the observed LWP (microwave) with its adiabatic counterpart (LWP_{ad}). Following Albrecht *et al.* [1990], LWP_{ad} was calculated as

$$LWP_{ad} = \frac{\rho_a}{\rho_w} \Gamma_{ad} \cdot \frac{\Delta Z^2}{2} \tag{1}$$

where ρ_a and Γ_{ad} are the mean in-cloud air density and adiabatic lapse rate, respectively, and ΔZ is the cloud thickness. Equation (1) is obtained by vertically integrating the adiabatic liquid water content, which is in turn a linear function of height. Temperature and pressure profiles for ρ_a and Γ_{ad} calculations were taken from radiosondes matched to the HSRL cloud base and radar cloud top height pair to within 4 h. A more restrictive temporal collocation criterion produced similar results but with a reduced number of matched samples. We selected the period June through July 2013, when all the active sensors were operational and radiosondes, needed for computing Γ_{ad} , were launched frequently.

Figure 1 compares 10 min averaged MWR-determined LWP and LWP_{ad} , from samples for boundary layer clouds only (top heights from the radar below 3 km) that are overcast (cloud frequency > 0.95) and have values between 15 and 250 g/m^2 and precipitation frequencies less than 0.1, to guarantee good quality MWR LWP. We note that at 15 g/m^2 , the LWP has an associated error of around 30%, which is a substantial improvement over the uncertainties for two-channel microwave radiometer LWP retrievals [Cadeddu *et al.*, 2013]. The linear correlation of 0.85 with a small bias (11.8 g/m^2) suggests a near-adiabatic behavior. The 1:1 relationship between adiabatic and MWR LWP implies that the effect of cloud top entrainment is modest because the entrainment rate is small and/or the boundary layer turbulence is able to partially offset the

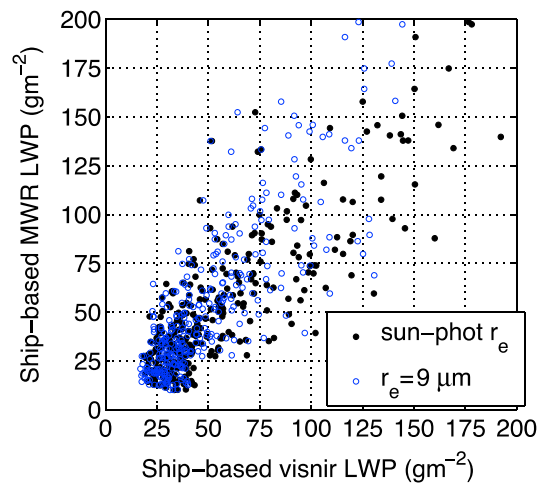


Figure 2. Ship-based comparison between Sun photometer (Sun-phot) LWP, derived from r_e and τ , and from MWR. Blue circles correspond to Sun photometer LWP derived from τ assuming a constant $r_e = 9 \mu\text{m}$.

estimates was high ($r = 0.99$). As a result, the ceilometer adiabatic calculations averaged 29.6 g/m^2 lower than those determined from the HSRL, implying an implausible cloud superadiabaticity. Given the HSRL's good calibration and its high sensitivity to water droplets, the HSRL cloud base height detection was used, as it was deemed more reliable.

3.1. Ship-Based Sun Photometer and Microwave Liquid Water Path Consistency

An advantage of the MAGIC campaign is that the availability of multi-instrument measurements allows testing of the physical consistency among different retrievals. Figure 2 (black dots) compares 10 min averaged LWP derived from the MWR and the Sun photometer (Sun-phot) LWP values for overcast samples with LWP less than 250 g/m^2 . These retrievals have a positive linear correlation coefficient of 0.86 and a Sun-phot LWP positive bias of 6.7 g m^{-2} , although the relationship is rather scattered. Since Sun-phot LWP is a function of both τ and r_e , we isolate the effect of τ on LWP by simply assuming a constant r_e at $9 \mu\text{m}$, consistent with typical values found over the study region [e.g., Lu *et al.*, 2007, Table 1], and recalculate the corresponding LWP. The comparison against MWR LWP (Figure 2, blue circles) shows a linear correlation coefficient of 0.82 and a Sun-phot LWP positive bias of 1.2 g m^{-2} , which are comparable to those obtained when using Sun-phot r_e . These results indicate that the good correlation between Sun-phot and MWR LWP is mainly due to Sun-phot τ , with a small correlation improvement attributed to Sun-phot r_e . We note that retrieving r_e from zenith radiance measurements is more challenging than retrieving τ , because the competing processes between radiance reduction from stronger absorption for larger droplets and radiance enhancement due to stronger forward scattering weaken the sensitivity of zenith radiance to cloud droplet size, and makes it harder to improve the r_e retrieval accuracy [Chiu *et al.*, 2012]. Therefore, given the good agreement between the MWR LWP and Sun photometer τ , they will be further applied to evaluate satellite observations, as well as for calculating N_d .

3.2. Consistency of Satellite and Ship-Based Cloud Retrievals

Before determining consistency between ship and satellite-based aerosol-cloud interaction (ACI) metrics, we compare ship and satellite retrievals of cloud properties. Following the methodology in P15, we spatially average the satellite data to a common 20 km resolution. This is intended to provide a more robust screening of partially cloudy scenes by utilizing only grids with cloud cover exceeding 95%. To be consistent with the satellite resolution, the ship-based data were hourly averaged (equivalent to a 20–40 km distance traveled by the ship). The LWP comparisons in Figure 3a and Table 2 show a linear correlation coefficient between MODIS (GOES-15) and the ship-based LWP data of 0.96 (0.88) with a mean bias of 12 g/m^2 (12.7 g/m^2). A similar, positive bias was also reported over the southeast Pacific by Painemal and Zuidema [2011] and

cloud dilution. Mean LWP values of 83.3 and 94.87 g/m^2 from MWR and the adiabatic computation, respectively, are equivalent to a subadiabatic fraction, defined as the ratio of the MWR LWP to LWP_{ad} , of 0.88. This subadiabatic fraction is close to values reported by Zuidema *et al.* [2012] in the southeast Pacific using an airborne microwave radiometer, where median fractions ranged between 0.86 and 0.96. It is important to clarify that the adiabatic fraction is prone to uncertainties due to the combined errors in the radar and HSRL cloud boundary detections. For instance, we computed a Gaussian propagating error near 9.4 g/m^2 for the mean LWP_{ad} caused solely by limitations in the instruments' vertical bin size resolution (7.5 and 30 m for the HSRL and radar, respectively).

LWP_{ad} was also derived using the ceilometer cloud base height (not shown). This height averaged 47.5 m greater than that determined from the HSRL, even though the correlation between both

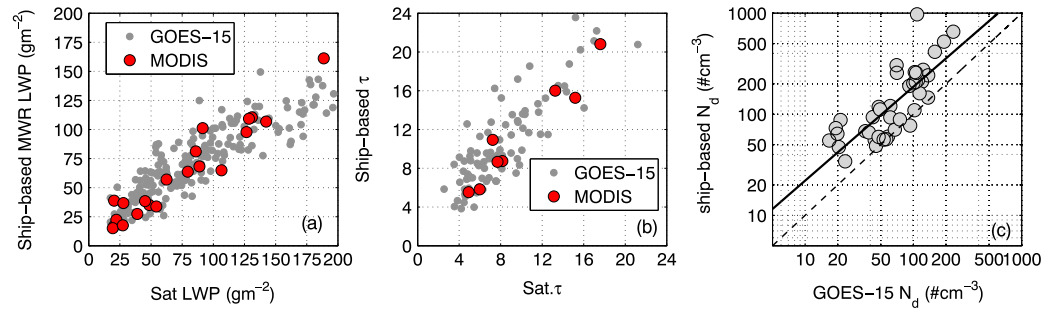


Figure 3. Scatterplot between GOES-15 (gray) and MODIS (red) satellite retrievals against their ship-based counterparts for (a) liquid water path (LWP) and (b) aerosol optical depth (τ), and (c) GOES-15 cloud drop number concentration (N_d), with the solid line denoting the linear fit and the dashed line the 1:1 line.

Painemal *et al.* [2012]. Ship-based and satellite τ values are highly correlated (Figure 3b and Table 2), but with the satellite values negatively biased relative to the ship-based retrievals.

Given the near-adiabatic behavior of the clouds, we computed the ship-based N_d using the relationship in Painemal and Zuidema [2013]:

$$N_d(\text{LWP}, \tau) [\text{cm}^{-3}] = 0.058 [\text{g}^2 \text{cm}^{-6}] \cdot \frac{\Gamma_{\text{obs}}^{1/2}}{k} \cdot \frac{\tau^3}{\text{LWP}^{5/2}} \quad (2)$$

where Γ_{obs} is the observed stratification of the water content with height, and k is the ratio between the cube of the effective radius and the mean volume radius of the droplet size distribution. The units for Γ_{obs} and LWP in equation (2) are in $[\text{g}/\text{cm}^4]$ and $[\text{g}/\text{cm}^2]$, respectively. Here we use a constant $\Gamma_{\text{obs}} = 1.4 \text{ g}/\text{m}^3/\text{km}$ and $k = 0.88$, which are averaged values derived from aircraft data over the southeast Pacific during the VOCALS Regional Experiment [Painemal and Zuidema, 2011]. We reduce uncertainties in the retrievals due to thin clouds [e.g., Lim *et al.*, 2016] by limiting the analysis to samples with $\text{LWP} > 15 \text{ g}/\text{m}^2$.

Following a similar methodology, described in Painemal and Zuidema [2011], satellite N_d is computed, assuming r_e in [cm], as

$$N_d(r_e, \tau) [\text{cm}^{-3}] = 1.41 \times 10^{-6} [\text{cm}^{-1/2}] \cdot \frac{\tau^{1/2}}{r_e^{5/2}} \quad (3)$$

We apply equations (2) and (3) to the ship-based and satellite data, respectively, and compare ship-based and satellite N_d in Table 2 and Figure 3c. The GOES-15 and the ship-based N_d retrievals have a statistically significant (at 99% confidence level according to a Student's t test) high correlation (with linear correlation coefficient 0.78), especially considering the rather dissimilar equations used to compute N_d . Their scatterplot in Figure 3c shows a linear relationship on a log-log scale, and although the ship-based N_d tends to be larger than GOES-15, it is parallel to the 1-1 line (slope at 0.93), implying that these two quantities are only related by a constant factor. It is not possible to determine with the available measurements which N_d values better resemble the real ones. Moreover, despite the magnitude differences between ship-based and satellite data, their values are reasonable and consistent with the range of variability observed during aircraft field campaigns off the coast of California [e.g., Wang *et al.*, 2009]. The disagreement in terms of the absolute magnitude of N_d appears to be associated with satellite τ underestimate relative to the Sun photometer retrieval. For instance, if one assumes that τ is the only source of uncertainty, and GOES τ is 20.7% smaller than its

Table 2. Linear Correlation Mean Bias and Root-Mean-Square Deviation Between MODIS (GOES-15) Retrieved Values and Ship-Based Observations^a

Quantity	Linear Correlation Coefficient r	Mean Bias	Root-Mean-Square Deviation RMSD
LWP (g/m^2)	0.96 (0.88)	12, 13.4% (12.7, 16.8%)	18.9 (26.4)
τ	0.96 (0.83)	-1.46, -14% (-2.3, -20.7%)	2.03 (3.26)
N_d (cm^{-3})	-0.29 (0.78)	-154.3, -61% (-101, -56%)	261.3 (184.5)

^aCorrelations in bold are statistically significant at 99% confidence level according to a Student's t test.

ship-based counterpart (Table 2), it follows from equation (2) that GOES N_d is 50% smaller than the ship-based N_d , a result consistent with the actual mean bias. Even though the linear correlation coefficient between ship-based and MODIS N_d is small and negative (Table 2), the comparison is statistically insignificant because the statistics were calculated based on only six collocated samples.

3.3. Error Characterization

Since the intercomparison of several data sets and the ACI quantification entail the computation of slopes, we paid close attention to the calculation details. Instead of applying the standard least squares regression, we used the York fit regression [York *et al.*, 2004]. This iterative method provides symmetrical slopes in x and y and is less affected by outliers than the standard linear regression [Cantrell, 2008]. For calculating York-derived slopes, measurement/retrieval errors need to be specified and are documented as follows.

For estimating satellite N_d errors, we rely on comparisons over the southeast Pacific between 20 km averaged GOES-10 and aircraft microphysical observations. The root-mean-square error relative to the mean in Painemal *et al.* [2012] is approximately 30%, which is similar to the MODIS Gaussian error of 25% used in Painemal and Zuidema [2010]. For simplicity, we adopt a constant 30% error in N_d for both the GOES-15 and MODIS retrievals.

We estimate the error in the ship-based N_d by adopting a Gaussian propagation error methodology. This requires the uncertainty characterization of each term of equation (2). Sun photometer τ errors were estimated by adding randomly generated perturbations to the measurements during the retrieving process [Chiu *et al.*, 2012]. This procedure yielded an averaged error of 19% in both r_e and τ during MAGIC. Nevertheless, this value likely underestimates the overall error associated with the use of a 1-D radiative transfer (plane-parallel) model in the algorithm. An alternative error assessment was based on the comparison between synthetic cloud observations (from a large eddy simulation LES model with a horizontal resolution of 67 m) and plane-parallel cloud retrievals obtained from radiances simulated from the synthetic cloud scene [Chiu *et al.*, 2012]. This comparison yielded a root-mean-square difference (RMSD) between the retrieved τ and that from the LES close to 30%. We utilize this error in our calculation because it better reflects the challenges of retrieving τ with the Sun photometer.

Additionally, we use a 15% error in the microwave LWP, which is the upper error reported in Cadet *et al.* [2013] associated with the mean LWP during MAGIC. For the parameter k in equation (2), we use an uncertainty of 20%, a value that represents the spread of the k distribution measured for the southeast Pacific stratocumulus clouds during VOCALS [Painemal and Zuidema, 2011]. The error in Γ was estimated at 20%, which is slightly smaller than the standard deviation of the LWP subadiabatic fraction during MAGIC (30%), yet the contribution of Γ to the overall error is modest. The combined N_d Gaussian propagating error, calculated as the square root of the sum of the squared errors under the assumption that the individual errors are uncorrelated, is 100%, a value that can be substantially reduced by applying 10 min data averaging. This arbitrary temporal average allows enough samples in the averaging to reduce measurement errors while preserving part of the observational variance. Assuming 7 to 10 samples every 10 min (dictated by the availability of MWR data), the 10 min N_d error becomes $100\%/\sqrt{7} = 38\%$. This error does not consider other sources of uncertainty such as the dissimilar instrument fields of view and the validity of equation (2). These factors appear to explain why previous studies that applied similar N_d equations reported a high variability and at times very large N_d values not observed in in situ aircraft data [e.g., Lim *et al.*, 2016; McComiskey *et al.*, 2009].

For aerosol properties, we also use the 10 min coefficient of variation as the fractional error. This yields mean errors of 11% for CCN concentration, 9% for UHSAS accumulation mode aerosol concentration (diameters between 0.1 and 1.0 μm), and 25% for the dry nephelometer measurements, after applying the corrections described in section 4.3.

4. Results

4.1. Satellite N_d and Ship-Based CCN

ACI, defined as $\text{ACI}_{\text{CCN}} = \frac{\partial \ln(N_d)}{\partial \ln(\text{CCN})}$ and derived from satellite N_d and ship-based CCN, was examined in P15 for the full MAGIC deployment, with ACI_{CCN} around 0.9 for linear fits of the logarithm of the GOES-15 N_d versus

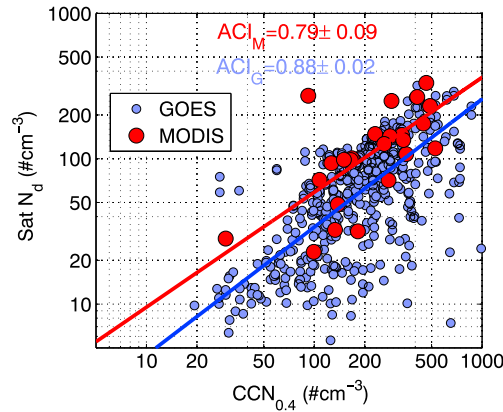


Figure 4. Scatterplot between $CCN_{0.4}$ and satellite N_d for MODIS (red) and GOES (blue). ACI_M and ACI_G are the slopes for MODIS and GOES-15.

the logarithm of the CCN concentration at 0.4% supersaturation ($CCN_{0.4}$). Here we perform a similar analysis for the May–August 2013 sampling period (spring–summer). Figure 4 depicts the relationship between satellite N_d from MODIS (red) and GOES-15 (blue) and $CCN_{0.4}$. The linear correlation coefficient of the logarithms of the two quantities is near 0.65 for both GOES-15 and MODIS. ACI_{CCN} for each satellite cloud data set is 0.88 ± 0.02 for GOES (ACI_G) and 0.79 ± 0.09 for MODIS (ACI_M).

Even though satellite data offer a valuable alternative when other data sets are unavailable, the use of ship observations is more appropriate because they are spatially/temporally collocated with the CCN measurements, and the instruments sampled cloud structures that were much smaller than those observed by satellites.

4.2. Ship-Based Computation of Aerosol-Cloud Interactions

Figure 5a shows the relationship between 10 min averaged $CCN_{0.4}$ and N_d using overcast samples, defined as those samples with ceilometer cloud frequency higher than 0.95 (gray circles), to reduce the effect of 3-D radiative effects near the cloud edges (at visible/near-infrared wavelengths) and clear-sky contamination in the retrievals. The red circles correspond to samples with precipitation occurrence frequency more than 10%. Additionally, the $CCN_{0.3}$ - N_d data for nonprecipitating samples are also depicted (blue open circles). The overall $CCN_{0.4}$ - N_d correlation is high and statistically significant ($r = 0.79$), and the slope of the logarithm of ship-based N_d versus logarithm of $CCN_{0.4}$ (ACI_{CCN}) is 1.39 ± 0.10 , with ± 0.10 denoting the standard error of the slope. ACI_{CCN} slightly decreases to 1.30 ± 0.13 when only nonprecipitating samples are considered. These values are slightly greater than the physical upper limit of 1.0, at which the fractional change in aerosol is linked to an equivalent fractional change in N_d . It is plausible that the calculations are not robust due to the small number of samples. This is mainly due to the CCN counter 10 min sampling cycle with constant supersaturation. We repeated the nonprecipitating ACI calculation but using $CCN_{0.3}$ instead and found a smaller value at 0.98 ± 0.12 , which is within the expected physical values. It is unclear why both $CCN_{0.4}$ and $CCN_{0.3}$ do not yield the same ACI, especially when considering that both CCN measurements are strongly correlated at 0.98 with a logarithmic slope of 1.0. As previously mentioned, the small number of samples (Table 3), due to gaps in the radar data set, might be the reason for the ACI disagreement. When repeating the ACI calculation using all the available samples irrespective of the radar data availability, the number of points increases more than 35%, and the different CCN-based calculations start to converge, with ACI at 0.97 and 1.18 for $CCN_{0.3}$ and $CCN_{0.4}$, respectively. Similarly, the use of CCN at 0.2% ($CCN_{0.2}$) produces an $ACI = 1.11 \pm 0.14$. We did not report the $CCN_{0.2}$ -based ACI for nonprecipitating scenes because the number of samples was small (less than 15) and the $CCN_{0.2}$ - N_d correlation was statistically insignificant.

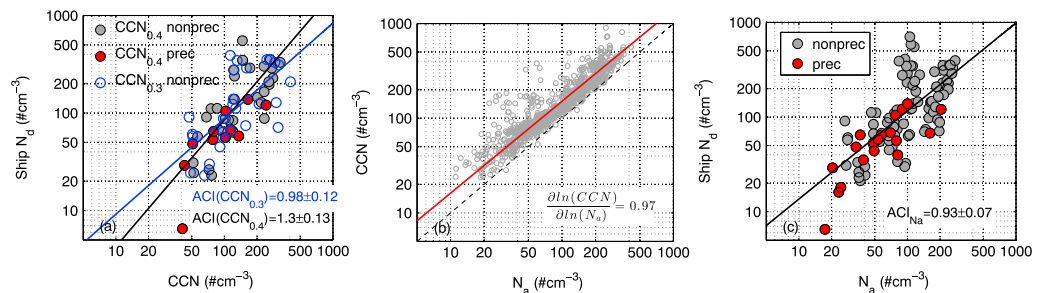


Figure 5. Ten-minute averaged relationships for (a) N_d and $CCN_{0.4}$ (gray and red), and $CCN_{0.3}$ and N_d (blue open circles, nonprecipitating samples) (b) $CCN_{0.4}$, and accumulation mode aerosol N_a , and (c) N_d versus N_a . Red circles are samples with precipitation frequency of occurrence of more than 10%. ACI is reported for nonprecipitating samples only.

Table 3. ACI Determined Using 10 min Averaged Ship-Based N_d and Different Aerosol Properties α^a

Aerosol Property	ACI _{CCN}	Correlation (Log Scale)	Number of Matched Samples
CCN _{0.4}	1.39 (1.3)	0.79 (0.76)	54 (36)
CCN _{0.3}	0.96 (0.98)	0.65 (0.65)	35 (28)
$N_a^{0.97}$	1.04 (0.95)	0.72 (0.66)	104 (85)
$\sigma_{\text{ext}}^{0.87}$	1.15 (1.1)	0.73 (0.71)	61 (48)

^aParentetical values correspond to statistics after removing samples with precipitation frequency >0.1. All correlations are statistically significant at 99% confidence level according to a Student's *t* test.

We further constrain the aerosol-cloud interaction metric by using the accumulation mode aerosol concentration (N_a , diameters between 100 nm and 1.0 μm) derived from the UHSAS and compute a N_a -based ACI as $\text{ACI}_{N_a} = \frac{\partial \ln(N_d)}{\partial \ln(N_a)}$. The use of N_a is reasonable as the fraction of aerosols activated into CCN is typically high for aerosol diameters larger than 100 nm and supersaturations higher than 0.2% [e.g., *Bougiatioti et al.*, 2011]. One major advantage of using N_a is that the number of samples is double than that for CCN. As a consistency check, we show in Figure 5b the relationship between N_a and CCN_{0.4} for all-sky observations during both day and night. The correlation between both aerosol quantities is high ($r = 0.90$), and the slope of the logarithm of CCN_{0.4} versus logarithm of N_a is near 1.0 (0.97). When the N_d -CCN analysis of Figure 5a was repeated but used N_a instead of CCN (Figure 5c), the correlation is high ($r = 0.72$) and ACI_{N_a} is also high at 1.00 ± 0.05 , the physical upper limit. The nonprecipitating ACI_{N_a} values slightly decrease to 0.93 ± 0.07 , mostly due to the effect of removing very low concentrations of N_a and N_d . After using the slope in Figure 5b to infer CCN_{0.4} from N_a , the equivalent ACI_{CCN}

$$\text{ACI}_{\text{CCN}} = \frac{\partial \ln(N_d)}{\partial \ln(N_a)} \cdot \frac{\partial \ln(N_a)}{\partial \ln(\text{CCN})} = \frac{\text{ACI}_{N_a}}{0.97} \quad (4)$$

becomes 1.03 and 0.96 for all and nonprecipitating samples, respectively.

We also repeated the previous analysis but used hourly averages to emulate the spatial resolution of the satellite. We compare N_d against both CCN_{0.4} and N_a (Figure 6). As in Figure 5, the samples having more precipitation occurrences are associated with low concentrations of aerosols and N_d . The slopes are not different from their 10 min counterparts, and overall, their ACI_{CCN} and ACI_{N_a} values are near 1.0. These slopes are only 10%–20% greater than those derived from satellite N_d and ship-based CCN_{0.4}.

4.3. Aerosol Scattering (σ_{scatt}), Extinction Coefficient (σ_{ext}), and N_d Slope

Shinozuka et al. [2015] evaluated the use of dry aerosol scattering (σ_{scatt}) and extinction (σ_{ext}) coefficients as proxies for CCN concentrations. In their study, CCN concentration is assumed to be directly proportional to $\sigma_{\text{ext}}^\beta$ with β between 0.5 and 0.9, depending on the geographical region considered. We used this relationship with MAGIC data to compute β and evaluate the use of σ_{ext} in calculating the ACI metric. Aerosol hygroscopic growth can result in much larger diameters of particles and thus substantially alter the scattering properties.

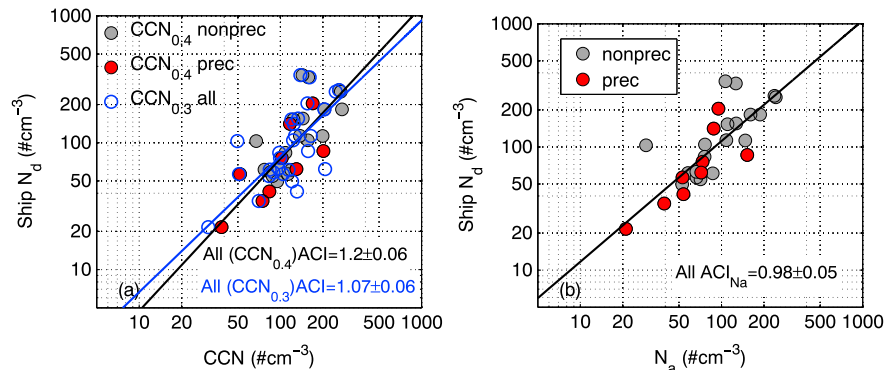


Figure 6. Hourly averaged relationship between (a) CCN_{0.4} and N_d (gray and red) and CCN_{0.3} and N_d (open blue circles), and (b) N_a and N_d . Red circles are samples with precipitation frequency of occurrence of more than 10%.

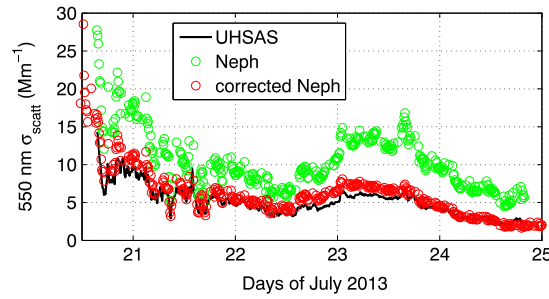


Figure 7. The 550 nm light scattering coefficient time series during a July leg (Leg 15A, California-Hawaii). Green circles denote raw nephelometer measurements. Red circles are the corrected nephelometer σ_{dry} after applying the humidification factor correction. Solid black line is the Mie calculation derived using the UHSAS particle size distribution and refractive index at $1.53 + 0.0i$, typical of ammonium sulfate.

Thus, before the analysis was performed, a simple correction method was devised to convert the observed measurements of aerosol scattering coefficient made at relative humidity (RH) values near 70%, σ_{neph} , to dry scattering coefficients, σ_{dry} , the quantity that can be more directly related to aerosol number concentration. The method relies on a simple parameterization that relates the humidified-to-dry scattering coefficient ratio, $\sigma_{neph}/\sigma_{dry}$, defined as a humidification factor $f(RH)$, to RH using the expression reported by Gasso *et al.* [2000] over the northern Atlantic for a clean marine air mass:

$$f(RH) = 0.76 \cdot \left(1 - \frac{RH}{100}\right)^{-0.69} \quad (5)$$

The constant parameters in equation (5) can also be estimated with measurements of light scattering at low and high RH. Although a second nephelometer during MAGIC measured aerosol scattering at varying relative humidity, it did not perform as designed. With a very limited number of samples, we derived $f(RH)$ when at least one instrument measured at $RH < 45\%$ and we found a parameterization, $f(RH) = 0.73 \cdot \left(1 - \frac{RH}{100}\right)^{-0.63}$, which is similar to and partially confirms equation (5).

Even though it is not possible to fully evaluate how well equation (5) represents the conditions during MAGIC, we can test whether the corrected σ_{dry} is consistent with Mie calculations for a specific aerosol species. For this purpose, we used dry aerosol size distributions obtained from the UHSAS and assumed a refractive index of ammonium sulfate at $1.53 + 0.0i$ [Toon *et al.*, 1976], a value similar to that for sodium chloride (two dominant aerosol species in the marine boundary layer). Given that UHSAS only derives distributions for particles with optical diameters less than $1 \mu m$, we only used nephelometer observations when the instrument operated with a $1 \mu m$ cutoff.

Figure 7 shows the time series of scattering coefficients for a specific California-Hawaii transect. Green circles are the uncorrected nephelometer data at 550 nm, the corrected σ_{dry} is in red, and the Mie-calculated σ_{scatt} (based on UHSAS data) is in black. The agreement between σ_{dry} and the Mie-calculated values is remarkable, lending support to the use of the simple humidification factor. The figure also shows the magnitude of changes due to RH. At times, nephelometer data are two times greater than the corrected σ_{dry} . The linear correlation coefficient of the Mie-calculated dry scattering coefficient and the uncorrected σ_{scatt} is 0.86, while the bias is 2.87 (45%), with a RMSD of $4.95 M m^{-1}$ (79% relative to the mean). In contrast, the corrected σ_{scatt} (σ_{dry}) is on average only $0.39 M m^{-1}$ (11%) greater than the value of σ_{scatt} calculated from the UHSAS, with a linear correlation coefficient of 0.91, and a RMSD of 1.44. Because of the good agreement between the corrected σ_{dry} and σ_{scatt} , in the following analysis we will only make use of σ_{dry} .

Next, we compared 10 min averaged σ_{dry} with $CCN_{0.4}$ for σ_{dry} greater than $0.1 M m^{-1}$ to remove samples more affected by instrument noise. As in Shinozuka *et al.* [2015], the slope calculation between the logarithms of σ_{dry} and CCN is justified by the high-correlation coefficient (0.8) in Figure 8a. We adopted a σ_{dry} fractional error of 25% (coefficient of variation) for computing the York fit. This error is more than double that assumed by Shinozuka *et al.* [2015] and highlights the inherent challenges of ship deployments. We found a slope for the linear fit of the logarithms of $CCN_{0.4}$ and σ_{dry} to be $\beta = 0.82 \pm 0.01$ or equivalent to $CCN_{0.4} \propto \sigma_{dry}^{0.82}$. Since the aerosol extinction coefficient (σ_{ext}) is the physical quantity that can be more closely related to other aerosol remote sensing measurements, we repeated the analysis depicted in Figure 8a but for σ_{ext} . We first computed σ_{ext} by combining σ_{dry} and dry aerosol absorption coefficient (σ_{abs}) measured by the PSAP and previously converted to 550 nm absorption (section 2). Figure 8b shows the CCN - σ_{ext} relationship, which closely resembles that in Figure 8a, reflecting the weak aerosol absorption measured during MAGIC. The correlation of the logarithms of these two quantities is high ($r = 0.84$), and the slope slightly increases to $\beta = 0.87 \pm 0.01$ because, in logarithmic scale, inclusion of small σ_{abs} tends to mainly affect the lower left region of the CCN - σ_{ext}

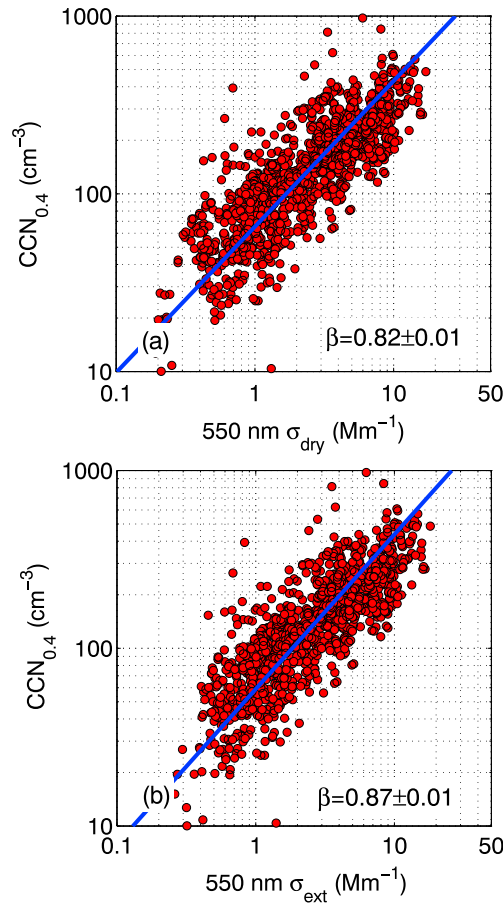


Figure 8. Scatterplot between $CCN_{0.4}$ and (a) dry aerosol scattering coefficient, and (b) extinction coefficient, β denotes the logarithmic slope (blue).

the boundary layer deepens and becomes less turbulently coupled. To confirm this finding, we computed ACI_{N_d} using nonprecipitating ship-based N_d and N_o for two groups with mean cloud base height less than and greater than the mean value of 835 m. In agreement with P15, it was found that the samples with shallower cloud bases (mean base at 577 m) have an overall linear correlation coefficient of 0.81 (logarithmic scale) and $ACI_{N_d} = 1.09$ (equivalent to $ACI_{CCN} = 1.12$), whereas the correlation and ACI_{N_d} decreases to 0.43 and 0.58 (equivalent to $ACI_{CCN} = 0.60$), respectively, for the deeper subcloud layer group (mean base at 1207 m). On average, the shallow subcloud layer (high ACI) is also well coupled; the cloud base height and lifting condensation level difference is 146 m, 432 m less than that for the deeper layer. These findings lead us to hypothesize that the boundary layer depth and the level of turbulent coupling determine how representative aerosol surface measurements are of those expected near the cloud base, where CCN activation typically occurs.

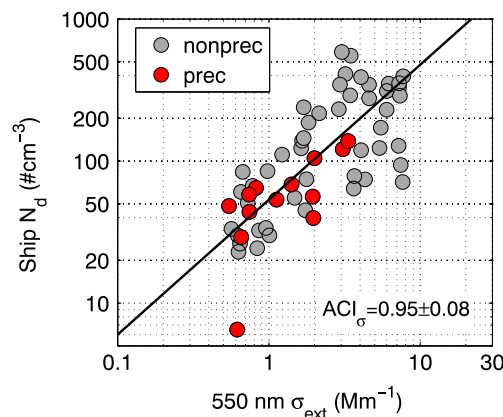


Figure 9. Scatterplot between 10 min averaged N_d and $550\text{ nm } \sigma_{ext}$. ACI_σ is reported for nonprecipitating samples only.

scatterplot by shifting it to the right. This factor $\beta = 0.87$ is similar to that found for ground-based ARM observations over the Azores/Graciosa Island in *Shinozuka et al.* [2015] of 0.83 (weight averaged by frequency of occurrence). This agreement is likely due to the similarities of these two marine boundary layer regimes in terms of their aerosol composition.

Having a way to relate σ_{ext} to CCN, we utilize σ_{ext} to derive $ACI_\sigma = \frac{\partial \ln(N_d)}{\partial \ln(\sigma_{ext})}$. We first show in Figure 9 the N_d - σ_{ext} relationship for 10 min averaged data. The logarithmic-scale linear correlation coefficient is 0.73 and the σ_{ext} -CCN slope (ACI_σ) is 1.00 ± 0.07 and 0.95 ± 0.08 for all and for precipitating samples, respectively. Using the exponent β , we can obtain the conversion from ACI_σ to ACI_{CCN} as $ACI_{CCN} = \frac{\partial \ln(N_d)}{\partial \ln(\sigma_{ext})} \cdot \frac{\partial \ln(\sigma_{ext})}{\partial \ln(CCN)}$ = $\frac{ACI_\sigma}{\beta}$. This yields equivalent ACI_{CCN} of 1.15 and 1.10 for all and nonprecipitating samples, respectively.

5. Discussion

5.1. Boundary Layer Deepening, Decoupling, and Aerosol Vertical Structure

Analysis of ACI_{CCN} variability along the westward transects using GOES N_d and ship-based CCN during the full MAGIC deployment in P15 showed that ACI values calculated from CCN concentration tend to decrease westward, as LWP decreases [*Painemal et al.*, 2016] and the boundary layer deepens and becomes less turbulently coupled. To confirm this finding, we computed ACI_{N_d} using nonprecipitating ship-based N_d and N_o for two groups with mean cloud base height less than and greater than the mean value of 835 m. In agreement with P15, it was found that the samples with shallower cloud bases (mean base at 577 m) have an overall linear correlation coefficient of 0.81 (logarithmic scale) and $ACI_{N_d} = 1.09$ (equivalent to $ACI_{CCN} = 1.12$), whereas the correlation and ACI_{N_d} decreases to 0.43 and 0.58 (equivalent to $ACI_{CCN} = 0.60$), respectively, for the deeper subcloud layer group (mean base at 1207 m). On average, the shallow subcloud layer (high ACI) is also well coupled; the cloud base height and lifting condensation level difference is 146 m, 432 m less than that for the deeper layer. These findings lead us to hypothesize that the boundary layer depth and the level of turbulent coupling determine how representative aerosol surface measurements are of those expected near the cloud base, where CCN activation typically occurs.

To evaluate this hypothesis, we use vertically resolved HSRL measurements of particle backscatter cross section per unit volume (σ_{back}). Although in principle, HSRL can provide aerosol

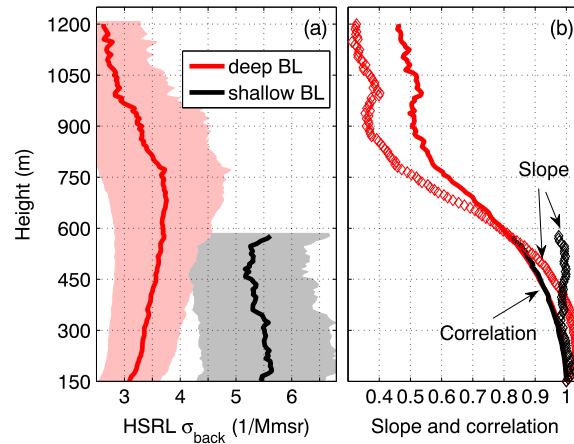


Figure 10. (a) Below-cloud particle backscatter cross section per unit volume (σ_{back}) from HSRL. Width of shaded area denotes half standard deviation. (b) Linear correlation (solid) and slope (diamonds) in logarithmic scale between 150 m backscatter ($\sigma_{back}(150\text{ m})$) and levels above (solid lines). Red and black lines are statistics derived from samples with cloud base below and above 835 m (deep and shallow boundary layers, BL, respectively). The profiles extend up to the mean cloud base height.

the role of the aerosol vertical structure in the context of the HSRL σ_{back} . That is, the covariability in the subcloud layer backscatter cross section as a function of height $\sigma_{back}(\sigma_{back}(z))$ is analyzed with respect to the lowest HSRL measurement at 150 m ($\sigma_{back}(150\text{ m})$), which is in turn used as a surrogate for near-surface aerosol observation. We first show in Figure 10a the mean HSRL $\sigma_{back}(z)$ profiles for the shallow and deep boundary layers, previously defined as those samples with cloud bases lower and higher than 835 m, respectively. These profiles were created after removing HSRL retrievals above the cloud base. The mean σ_{back} for the shallow composite (black) is greater than its deep composite counterpart (red) over the comparable height range, consistent with greater anthropogenic contributions near the coast, where the boundary layer is also shallower (P15). Next, we correlate $\sigma_{back}(z)$ with $\sigma_{back}(150\text{ m})$ and calculate its logarithmic slope, $\partial \ln(\sigma_{back}(150\text{ m})) / \partial \ln(\sigma_{back}(z))$, using an iteratively reweighted least squares fit with a bi-square weighting function to reduce the effect of outliers [Street et al., 1988]. As expected, $\sigma_{back}(z)$ correlates well with $\sigma_{back}(150\text{ m})$ for both shallow and deep boundary layers at elevations below 450 m, with values of the linear correlation coefficient greater than 0.9 (Figure 10b, solid black and red, respectively). The relationship becomes more scattered, and the correlation decreases to below 0.5 for heights above 900 m, near the cloud base in the deep boundary layer case. On the other hand, the slope is near unity below 400 m for both groups (diamonds), although for the shallow-layer case, values near unity are observed throughout the subcloud layer. In contrast, the slope starts to decrease in the deep boundary layer above 450 m, reaching a minimum near 0.4 at 900 m. These findings demonstrate that in deep boundary layers, the use of surface aerosol observations would tend to yield ACI indices and correlation coefficients less than those calculated using near cloud base aerosol measurements.

5.2. Ship-Based ACI Calculations

One limitation of this study is the use of N_d computed under the assumption of a near-adiabatic cloud model. We partially validated this assumption by showing a strong linearity between adiabatic and measured LWP. On the other hand, since we are mostly interested in the slope of N_d with respect to a given aerosol property rather than N_d absolute values, we argue that these slopes reduce the impact of N_d uncertainties and assumptions about the cloud microphysical structure, whereas the strong linear correlations support the computation of slopes. A second aspect is that we did not stratify our calculation as a function of LWP as in previous studies [e.g., Painemal and Zuidema, 2013; McComiskey and Feingold, 2012]. Although accounting for LWP is essential for radiative transfer computations of the indirect effect, N_d is weakly correlated with LWP ($r = -0.2$) and at least from the N_d -aerosol slope calculation viewpoint, LWP stratification is unnecessary.

extinction retrievals, these measurements are prone to several uncertainties (section 2). Given the relatively homogeneous σ_{ext} to σ_{back} ratio (lidar ratio) in marine environments [e.g., Burton et al., 2012], σ_{back} should capture the variability in σ_{ext} . In terms of near-surface observation, σ_{ext} derived from the nephelometer and PSAP operated at the 10 μm cut-off diameter mode, is a measurement physically comparable to that retrieved from HSRL. Unfortunately, the nephelometer did not measure at the ambient relative humidity, and thus further corrections would be necessary to account for the disparity between instrument and ambient humidity. The adequacy of such a correction is not possible to test, for instance, with Mie calculations, because the UHSAS did not determine the aerosol size distribution, necessary for scattering computations, for diameters larger than 1 μm . We circumvent the limitations in the surface measurements by investigating the

Table 4. ACI_{CCN} Determined Using Hourly Averaged Ship-Based and Satellite N_d Combined With Different Aerosol Measurements α^a

$N_d-\alpha$	ACI_{CCN}	Correlation (Log Scale)	Number of Matched Samples
Hourly $N_d-CCN_{0.4}$	1.2	0.77	29
Hourly $N_d-CCN_{0.3}$	1.07	0.67	28
Hourly $N_d-N_a^{0.97}$	1.01	0.78	29
MODIS $N_d-CCN_{0.4} (N_a^{0.97})$	0.79 (0.97)	0.65 (0.69)	24 (31)
GOES-15 $N_d-CCN_{0.4} (N_a^{0.97})$	0.88 (0.92)	0.66 (0.71)	534/(626)

^aParentetical values were estimated by combining satellite N_d and $N_a^{0.97}$. All correlations are statistically significant at 99% confidence level according to a Student's t test.

The 10 min average ACI calculations using CCN, N_a , and σ_{ext} (after applying the regressions) are summarized in Table 3. As previously mentioned, all the aerosol observations yield ACI_{CCN} near 1.0, although $CCN_{0.4}$ and $CCN_{0.3}$ yield slightly greater values. Given the anthropogenic contribution from particles with diameters less than 70 nm in the CCN measurements during MAGIC, along with the reduced number of collocated samples, the CCN-based ACI calculation might be less robust. On the other hand, $N_a^{0.97}$ and $\sigma_{ext}^{0.85}$ produce very similar ACI_{CCN} values, because particle sizes larger than 100–200 nm typically dominated the light scattering during MAGIC [Seinfeld and Pandis, 2006].

The ship-based results in this study are comparable to those derived over the Southeast Pacific during the 2008 VOCALS Regional Experiment, where ACI values derived from in situ microphysical airborne probes ranged between 0.71 and 0.92, [Painemal and Zuidema, 2013; Zheng et al., 2011]. McComiskey and Feingold [2008] reported an ACI = 0.85 using measurements in Twohy et al. [2005] during the DYCOMS-II (Dynamics and Chemistry of Marine Stratocumulus-II) campaign over the northeast Pacific. In addition, averaged flight data during MASE reported by Daum et al. [2007, Figure 14a] yield and ACI \approx 1.07. Overall, aircraft studies over the eastern Pacific yield an ACI range of 0.71–1.07, which is in close agreement with ACI values calculated from MAGIC data.

5.3. Satellite and Ship-Based Observations

The observational disagreement between aerosol-cloud interaction calculations derived from different data sets has been in part associated with the dissimilar spatiotemporal scales inherent in each platform [e.g., McComiskey and Feingold, 2012]. Since data averaging leads to variance reduction, it has been hypothesized that the large satellite fields of view explain in part the lesser satellite ACI values and weaker correlations between satellite retrievals of aerosols and cloud microphysics. Nevertheless, our analysis shows that an ACI_{CCN} value of 0.88–0.92, based on combined satellite N_d and ship-based CCN and N_a , is only slightly less than the hourly averaged ship-based ACI_{CCN} of \sim 1.01–1.2 (Table 4). Moreover, ship-based 10 min and hourly calculations also agree well. These results suggest that for the overcast clouds having little precipitation reported in this study, the spatial variability is small, and thus satellite data yield results comparable to those from in situ observations. Based on these results, we speculate that an important and partially ignored source of disagreement between satellite-based and in situ calculations is the use of satellite aerosol optical depth (AOD) as a CCN concentration proxy. AOD is problematic, as it is a vertically integrated quantity and may not fully represent the aerosol variability in the boundary layer. A second issue is that a few large particles can dominate AOD while contributing little to CCN concentration. In addition, several artifacts can modulate the AOD-cloud covariability, having the potential to produce a spurious aerosol-cloud interaction signal (see discussion in P15). Even if AOD is used as a substitute for CCN, the nonlinear relationship $CCN \propto \tau_{A}^\epsilon$, with $\epsilon < 1$, [e.g., Andreae, 2009] would imply $\frac{\partial \ln(N_d)}{\partial \ln(AOD)} < \frac{\partial \ln(N_d)}{\partial \ln(CCN)}$

6. Conclusions

The MAGIC deployment provided an unprecedented data set of aerosol and cloud properties over the north-east Pacific boundary layer. We used remotely sensed MAGIC retrievals of cloud properties to compute N_d and quantify its covariability with CCN and aerosol concentrations. We found that the value of an aerosol-cloud interaction index defined by $ACI_{CCN} = \partial \ln(N_d) / \partial \ln(\alpha)$, with α denoting CCN concentration, N_a , or σ_{ext} , is high and is near the upper physical limit of 1.0. The results are robust, whether using either 10 min or

hourly averaged data. In addition, a reduction of up to 10% in ACI after removing precipitating samples is associated with the effect of filtering low CCN concentration and N_d in the regression computation. The high ACI and correlations derived here exceed those from a similar ARM deployment at Point Reyes on the California coast [McComiskey *et al.*, 2009], while the MAGIC N_d is smaller and more physical than those reported in Lim *et al.* [2016]. Unlike the aforementioned studies, the use of a narrow field-of-view Sun photometer and improved LWP retrievals from a three-channel MWR is likely the main reason for the aerosol-cloud consistency reported here [Lim *et al.*, 2016].

A remarkable finding is the agreement between ACI values derived using the satellite N_d and that determined from only ship-based values. While this result was prefigured in the good agreement between satellite and ship-based cloud retrievals, it is surprising that despite the different spatial samplings and retrieval algorithms, the satellite cloud microphysics reproduce the ship-based ACI, which is in turn consistent with aircraft measurements taken in other marine boundary layer regimes. This result is encouraging and provides evidence that in overcast scenes with favorable satellite viewing angles, satellite cloud products provide valuable microphysical information, especially when in situ data set is unavailable.

We note that due to the limitations of MAGIC ship-based deployments, this study is primarily based on the relationship between N_d and CCN for fixed values of supersaturation. A more rigorous study should account for the updraft magnitude and the associated supersaturation for each sampling for a better ACI quantification. Since we are only utilizing overcast samples with LWP greater than 15 g/m^2 (section 3), it is likely that the analysis is inadvertently biased toward measurements with stronger updrafts and supersaturations, for which $\text{CCN}_{0.3}$ and $\text{CCN}_{0.4}$ might be representative of the activated aerosols. Other factors unaccounted for in our study are the role of the cloud top entrainment in modifying N_d , precipitation, and the cloud vertical structure, especially when this departs from the assumptions that allow for N_d calculations using equations (2) and (3).

The use of vertically resolved aerosol properties from a HSRL opens new opportunities for the investigation of the aerosol indirect effect, in principle, enabling better estimates than those based on surface observations only, which suffer from limitations in deep and decoupled marine boundary layers. Ghan and Collins [2004] and Ghan *et al.* [2006] devised a method to derive CCN profiles using the relationship between surface CCN and lidar backscatter cross section, combined with knowledge of the humidification factor. Our analysis supports the applicability of the Ghan and Collins method for surface-based aerosol extinction. To further extend the method for use with HSRL, it would be desirable to have accurate aerosol extinction retrievals, vertical profiles of CCN, relative humidity, and information about the aerosol species that can be used to select a proper humidification factor to help account for aerosol hygroscopic growth in the HSRL measurements.

Acknowledgments

This work was supported by the U.S. Department of Energy (DOE), Office of Science, Office of Biological and Environmental Research (OBER): DOE-BER Atmospheric Science Research Program (ASR) grants DE-FOA-0000885 (D. Painemal, P. Minnis, and C. Yost) and DE-SC0011666 (J.C. Chiu), Atmospheric Radiation Measurement Infrastructure Basic Energy Sciences, under contract DE-AC02-06CH11357 (M. Cadeddu), and DOE-BER under contract DE-SC00112704 (E.R. Lewis). C. Yost was also supported by the NASA CERES program. The MAGIC data set was downloaded from the ARM archive available at <http://www.archive.arm.gov/>. MODIS and GOES-15 retrievals are available at <http://www-pm.larc.nasa.gov> or upon request. We thank Horizon Lines and the Captain and crew of the Horizon *Spirit* for their support and hospitality during MAGIC. The constructive comments and suggestions provided by three anonymous reviewers are greatly appreciated.

References

- Albrecht, B., C. Fairall, D. Thomson, and A. White (1990), Surface-based remote sensing of the observed and the adiabatic liquid water content of stratocumulus clouds, *Geophys. Res. Lett.*, *17*, 89–92, doi:10.1029/GL017i001p00089.
- Anderson, T. L., et al. (1996), Performance characteristics of a high-sensitivity, three-wavelength total scatter/backscatter nephelometer, *J. Atmos. Oceanic Technol.*, *13*, 967–986.
- Andreae, M. O. (2009), Correlation between cloud condensation nuclei concentration and aerosol optical thickness in remote and polluted regions, *Atmos. Chem. Phys.*, *9*, 543–556, doi:10.5194/acp-9-543-2009.
- Bond, T. C., T. L. Anderson, and D. Campbell (1999), Calibration and intercomparison of filter-based measurements of visible light absorption by aerosols, *Aerosol Sci. Technol.*, *3*(6), 582–600, doi:10.1080/027868299304435.
- Bougiatioti, A., A. Nenes, C. Fountoukis, N. Kalivitis, S. N. Pandis, and N. Mihalopoulos (2011), Size-resolved CCN distributions and activation kinetics of aged continental and marine aerosol, *Atmos. Chem. Phys.*, *11*, 8791–8808, doi:10.5194/acp-11-8791-2011.
- Burton, S. P., R. A. Ferrare, C. A. Hostetler, J. W. Hair, R. R. Rogers, M. D. Obland, C. F. Butler, A. L. Cook, D. B. Harper, and K. D. Froyd (2012), Aerosol classification using airborne High Spectral Resolution Lidar measurements—Methodology and examples, *Atmos. Meas. Tech.*, *5*, 73–98, doi:10.5194/amt-5-73-2012.
- Cadeddu, M. P., J. C. Lijegren, and D. D. Turner (2013), The Atmospheric radiation measurement (ARM) program network of microwave radiometers: Instrumentation, data, and retrievals, *Atmos. Meas. Tech.*, *6*, 2359–2372, doi:10.5194/amt-6-2359-2013.
- Cai, Y., D. Montague, W. Mooiweer-Bryan, and T. Deshler (2008), Performance characteristics of the ultra-high-sensitivity aerosol spectrometer for particles between 55 and 800 nm: Laboratory and field studies, *J. Aerosol Sci.*, *39*(9), 759–769, doi:10.1016/j.jaerosci.2008.04.007.
- Cantrell, C. A. (2008), Technical note: Review of methods for linear least-squares fitting of data and application to atmospheric chemistry problems, *Atmos. Chem. Phys.*, *8*, 5477–5487.
- Carslaw, K. S., et al. (2013), Large contribution of natural aerosols to uncertainty in indirect forcing, *Nature*, *503*, 67–71.
- Chiu, J. C., C.-H. Huang, A. Marshak, I. Slutsker, D. M. Giles, B. N. Holben, Y. Knyazikhin, and W. J. Wiscombe (2010), Cloud optical depth retrievals from the Aerosol Robotic Network (AERONET) cloud mode observations, *J. Geophys. Res.*, *115*, D14202, doi:10.1029/2009JD013121.

- Chiu, J. C., A. Marshak, C.-H. Huang, T. Várnai, R. J. Hogan, D. M. Giles, B. N. Holben, E. J. O'Connor, Y. Knyazikhin, and W. J. Wiscombe (2012), Cloud droplet size and liquid water path retrievals from zenith radiance measurements: Examples from the atmospheric radiation measurement program and the aerosol robotic network, *Atmos. Chem. Phys.*, *12*, 10,313–10,329, doi:10.5194/acp-12-10313-2012.
- Chiu, J.-Y. C., L. Gregory, R. Wagener (2016), *MAGIC Cloud Properties From Zenith Radiance Data Final Campaign Summary*, United States: DOE ARM Clim. Res. Facility, Pacific Northwest Natl. Lab., Richland, Washington, doi:10.2172/1242830.
- Daum, P., Y. Liu, R. McGraw, Y. Lee, J. Wang, G. Senum, and M. Miller (2007), *Microphysical Properties of Stratus/Stratocumulus Clouds During the 2005 Marine Stratus/Stratocumulus Experiment (MASE)*, Rep. BNL-77935-2007-JA, Brookhaven Natl. Lab., Upton, New York.
- Eloranta, E. W. (2005), High spectral resolution lidar, in *Lidar: Range-Resolved Optical Remote Sensing of the Atmosphere*, Springer Ser. in Opt. Sci., edited by K. Weitkamp, pp. 143–163, Springer, New York.
- Fielding, M. D., J. C. Chiu, R. J. Hogan, G. Feingold, E. Eloranta, E. J. O'Connor, and M. P. Cadetdu (2015), Joint retrievals of cloud and drizzle in marine boundary layer clouds using ground-based radar, lidar and zenith radiances, *Atmos. Meas. Tech.*, *8*, 2663–2683, doi:10.5194/amt-8-2663-2015.
- Gasso, S., et al. (2000), Influence of humidity on the aerosol scattering coefficient and its effect on the upwelling radiance during ACE-2, *Tellus Ser. B*, *52*, 546–567.
- Ghan, S. J., and D. R. Collins (2004), Use of in situ data to test a Raman lidar-based cloud condensation nuclei remote sensing method, *J. Atmos. Oceanic Technol.*, *21*, 387–394.
- Ghan, S. J., et al. (2006), Use of in situ cloud condensation nuclei, extinction, and aerosol size distribution measurements to test a method for retrieving cloud condensation nuclei profiles from surface measurements, *J. Geophys. Res.*, *111*, D05S10, doi:10.1029/2004JD005752.
- Hegg, D. A., D. S. Covert, H. H. Jonsson, and R. K. Woods (2012), A simple relationship between cloud drop number concentration and precursor aerosol concentration for the regions of Earth's large marine stratocumulus decks, *Atmos. Chem. Phys.*, *12*, 1229–1238, doi:10.5194/acp-12-1229-2012.
- Hildebrand, P. H., and R. Sekhon (1974), Objective determination of the noise level in Doppler spectra, *J. Appl. Meteorol.*, *13*, 808–811, doi:10.1175/1520-0450(1974)013<0808:ODOTNL>2.0.CO;2.
- Hudson, J. G., S. Noble, and V. Jha (2010), Stratus cloud supersaturations, *Geophys. Res. Lett.*, *37*, L21813, doi:10.1029/2010GL045197.
- Kollias, P. E. E., et al. (2016), Development and applications of ARM millimeter-wavelength cloud radars, *Meteorol. Monogr.*, *57*, 17.1–17.19, doi:10.1175/AMSMONOGRAPH5-D-15-0037.1.
- Lewis, E. R., and J. Teixeira (2015), Dispelling clouds of uncertainty, *Eos Trans. AGU*, *96*, doi:10.1029/2015EO031303.
- Lim, K.-S. S., L. Riihimäki, J. M. Comstock, B. Schmid, C. Sivaraman, Y. Shi, and G. M. McFarquhar (2016), Evaluation of long-term surface-retrieved cloud droplet number concentration with in situ aircraft observations, *J. Geophys. Res. Atmos.*, *121*, 2318–2331, doi:10.1002/2015JD024082.
- Lu, M.-L., W. C. Conant, H. H. Jonsson, V. Varutbangkul, R. C. Flagan, and J. H. Seinfeld (2007), The Marine Stratus/Stratocumulus Experiment (MASE): Aerosol-cloud relationships in marine stratocumulus, *J. Geophys. Res.*, *112*, D10209, doi:10.1029/2006JD007985.
- McComiskey, A., and G. Feingold (2008), Quantifying error in the radiative forcing of the first aerosol indirect effect, *Geophys. Res. Lett.*, *35*, L02810, doi:10.1029/2007GL032667.
- McComiskey, A., and G. Feingold (2012), The scale problem in quantifying aerosol indirect effects, *Atmos. Chem. Phys.*, *12*, 1031–1049, doi:10.5194/acp-12-1031-2012.
- McComiskey, A., G. Feingold, A. S. Frisch, D. D. Turner, M. A. Miller, J. C. Chiu, Q. Min, and J. A. Ogren (2009), An assessment of aerosol-cloud interactions in marine stratus clouds based on surface remote sensing, *J. Geophys. Res.*, *114*, D09203, doi:10.1029/2008JD011006.
- Miller, M. A., K. Nitschke, T. P. Ackerman, W. R. Ferrrell, N. Hickmon, and M. Ivey (2016), The ARM mobile facilities, *Meteorol. Monogr.*, *57*, 9.1–9.15.
- Minnis, P., et al. (2008), Near-real time cloud retrievals from operational and research meteorological satellites, *Proc. SPIE Int. Soc. Opt. Eng.*, *7107*, 710703, doi:10.1117/12.800344.
- Minnis, P., et al. (2010), CERES Edition 3 cloud retrievals, AMS 13th Conf. Atmos. Rad., Portland, OR, June 27 – July 2, 5.4, 7 pp.
- Minnis, P., et al. (2011), CERES Edition-2 cloud property retrievals using TRMM VIRS and Terra and Aqua MODIS data. Part I: Algorithms, *IEEE Trans. Geosci. Remote Sens.*, *49*(11), 4374–4400, doi:10.1109/TGRS.2011.2144601.
- Painemal, D., and P. Zuidema (2010), Microphysical variability in southeast Pacific Stratocumulus clouds: Synoptic conditions and radiative response, *Atmos. Chem. Phys.*, *10*, 6255–6269, doi:10.5194/acp-10-6255-2010.
- Painemal, D., and P. Zuidema (2011), Assessment of MODIS cloud effective radius and optical thickness retrievals over the southeast Pacific with VOCALS-REx in situ measurements, *J. Geophys. Res.*, *116*, D24206, doi:10.1029/2011JD016155.
- Painemal, D., and P. Zuidema (2013), The first aerosol indirect effect quantified through airborne remote sensing during VOCALS-REx, *Atmos. Chem. Phys.*, *13*, 917–931.
- Painemal, D., P. Minnis, J. K. Ayers, and L. O'Neill (2012), GOES-10 microphysical retrievals in marine warm clouds: Multi-instrument validation and daytime cycle over the southeast Pacific, *J. Geophys. Res.*, *117*, D19212, doi:10.1029/2012JD017822.
- Painemal, D., P. Minnis, and M. Nordeen (2015), Aerosol variability, synoptic-scale processes, and their link to the cloud microphysics over the northeast Pacific during MAGIC, *J. Geophys. Res. Atmos.*, *120*, 5122–5139, doi:10.1002/2015JD023175.
- Painemal, D., T. Greenwald, M. Cadetdu, and P. Minnis (2016), First extended validation of satellite microwave liquid water path with ship-based observations of marine low clouds, *Geophys. Res. Lett.*, *43*, 6563–6570, doi:10.1002/2016GL069061.
- Quaas, J., et al. (2009), Aerosol indirect effects—General circulation model intercomparison and evaluation with satellite data, *Atmos. Chem. Phys.*, *9*, 8697–8717, doi:10.5194/acp-9-8697-2009.
- Roberts, G. C., and A. Nenes (2005), A continuous-flow streamwise thermal-gradient CCN chamber for atmospheric measurements, *Aerosol Sci. Technol.*, *39*(3), 206–221, doi:10.1080/027868290913988.
- Rosenfeld, D., S. Sherwood, R. Wood, and L. Donner (2014), Climate effects of aerosol-cloud interactions, *Science*, *343*(6169), 379–380, doi:10.1126/science.1247490.
- Seinfeld, J., and S. Pandis (2006), *Atmospheric Chemistry and Physics: From Air Pollution to Climate Change*, pp. 450, Wiley, N. J.
- Shinozuka, Y., et al. (2015), The relationship between cloud condensation nuclei (CCN) concentration and light extinction of dried particles: Indications of underlying aerosol processes and implications for satellite-based CCN estimates, *Atmos. Chem. Phys.*, *15*, 7585–7604, doi:10.5194/acp-15-7585-2015.
- Street, J. O., R. J. Carroll, and D. Ruppert (1988), A note on computing robust regression estimates via iteratively reweighted least squares, *Am. Stat.*, *42*, 152–154, doi:10.2307/2684491.
- Toon, O. B., J. B. Pollack, and B. N. Khare (1976), The optical constants of several atmospheric aerosol species: Ammonium sulfate, aluminum oxide, and sodium chloride, *J. Geophys. Res.*, *81*, 5733–5748, doi:10.1029/JC081i033p05733.

- Twohy, C. H., M. D. Petters, J. R. Snider, B. Stevens, W. Tahnk, M. Wetzel, L. Russell, and F. Burnet (2005), Evaluation of the aerosol indirect effect in marine stratocumulus clouds: Droplet number, size, liquid water path, and radiative impact, *J. Geophys. Res.*, *110*, D08203, doi:10.1029/2004JD005116.
- Wang, J., P. H. Daum, S. S. Yum, Y. Liu, G. I. Senum, M.-L. Lu, J. H. Seinfeld, and H. Jonsson (2009), Observations of marine stratocumulus microphysics and implications for processes controlling droplet spectra: Results from the Marine Stratus/Stratocumulus Experiment, *J. Geophys. Res.*, *114*, D18210, doi:10.1029/2008JD011035.
- York, D., N. Evensen, M. L. Martinex, and J. D. B. Delgado (2004), Unified equations for the slope, intercept, and standard errors of the best straight line, *Am. J. Phys.*, *72*, 367–375.
- Zheng, X., et al. (2011), Observations of the boundary layer, cloud, and aerosol variability in the southeast Pacific near-coastal marine stratocumulus during VOCALS-REx, *Atmos. Chem. Phys.*, *11*, 9943–9959, doi:10.5194/acp-11-9943-2011.
- Zhou, X., P. Kollias, and E. Lewis (2015), Clouds, precipitation and marine boundary layer structure during MAGIC, *J. Clim.*, doi:10.1175/JCLI-D-14-00320.1.
- Zuidema, P., D. Leon, A. Pazmany, and M. Cadeddu (2012), Aircraft millimeter-wave passive sensing of cloud liquid water and water vapor during VOCALS-REx, *Atmos. Chem. Phys.*, *12*, 355–369, doi:10.5194/acp-12-355-2012.